

pubs.acs.org/JACS Article

# In Situ Constructing the Kinetic Roadmap of Octahedral Nanocrystal Assembly Toward Controlled Superlattice Fabrication

Xin Huang, Jinlong Zhu, Binghui Ge, Frauke Gerdes, Christian Klinke, and Zhongwu Wang\*



Cite This: https://dx.doi.org/10.1021/jacs.0c12087



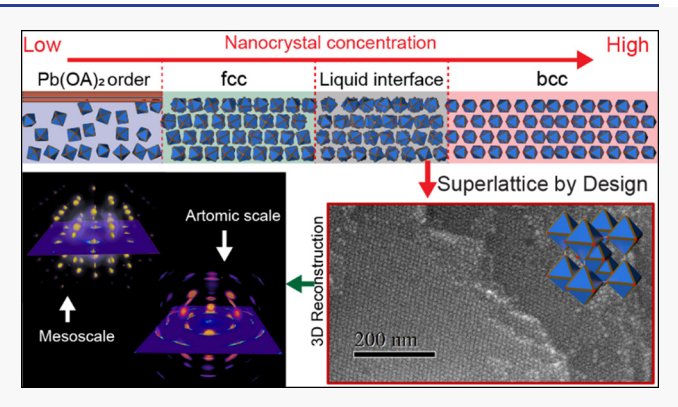
**ACCESS** 

III Metrics & More

Article Recommendations

Supporting Information

ABSTRACT: Crystallization and growth of anisotropic nanocrystals (NCs) into distinct superlattices were studied in real time, yielding kinetic details and designer parameters for scale-up fabrication of functional materials. Using octahedral PbS NC blocks, we discovered that NC assembly involves a primary lamellar ordering of NC-detached Pb(OA)<sub>2</sub> molecules on the front-spreading solvent surfaces. Upon a spontaneous increase of NC concentration during solvent processing, PbS NCs preferentially self-assembled into an orientation-disordered face-centered cubic (fcc) superlattice, which subsequently transformed into a bodycentered cubic (bcc) superlattice with single NC-orientational ordering across individual domains. Unlike the deformation-based transformation route claimed previously, this solid—solid phase



transformation involved a hidden intermediate formation of a lamellar-confined liquid interface at cost of the disassembly (melting) of small fcc grains. Such highly condensed and liquidized NCs recrystallized into the stable bcc phase with an energy reduction of 1.16  $k_{\rm B}T$ . This energy-favorable and high NC-fraction-driven bcc phase grew as a 2D film at a propagation rate of 0.74  $\mu$ m/min, smaller than the 1.23  $\mu$ m/min observed in the early nucleated fcc phase under a dilute NC environment. Taking such insights and defined parameters, we designed experiments to manipulate the NC assembly pathway and achieved scalable fabrication of a large/single bcc supercrystal with coherent ordering of NC translation and atomic plane orientation. This study not only provides a design avenue for controllable fabrication of a large supercrystal with desired superlattices for application but also sheds new light on the nature of crystal nucleation/growth and phase transformation by extending the lengths from the nanoscale into the atomic scale, molecular scale, and microscale levels.

# ■ INTRODUCTION

The nucleation and growth of crystalline solids occur ubiquitously in nature, but very little is known of how a crystal starts nucleating in a structure and grows large. 1,2 As this spontaneous process goes at a fast pace, it is also questionable of whether one additional event such as a phase transformation happens and how such an intermediate event changes the energy landscape and transforms the early nucleated lattice into another one.3 At the atomic and molecular levels, techniques with sufficient temporal and spatial resolutions in the simultaneous capture of the fast kinetic events over the course of the crystal nucleation and growth are still largely absent. This is typically true for the samples with largely extended dimensions and under realistic environments, once the real-world applications are taken into account.4-6 Nanocrystals (NCs) behave like atoms and can spontaneously self-assemble into periodically ordered structures so that NC assembly appears as an alternative platform and can be used to explore a rich variety of structures and polymorphs. With such designer atoms, experiments can be also controlled to innovate the applications of existing techniques with a penetration capability into large samples to

access the time and space domains in real materials processing for in situ study.  $^{8,9}$ 

NC assembly displays increased structural complexities as NCs change shape from isotropic to anisotropic. <sup>7,10-12</sup> As the simplest one, spherical NCs preferably crystallize in the close packing superlattice of either a face-centered cubic (fcc) or hexagonal close packing (hcp) lattice. <sup>13</sup> Once NCs become anisotropic, the emergent shapes introduce directional interaction forces, <sup>10</sup> driving NC assembly into a rich diversity of complex superlattices from open lattices of body-centered cubic (bcc) <sup>14</sup> and diamond <sup>15</sup> to porous clathrate <sup>16,17</sup> and topological object <sup>18</sup> or even aperiodic quasicrystal. <sup>19,20</sup> The delicate tuning of directional interaction forces between shaped NCs through the modification of the surface molecular

Received: November 18, 2020



decoration and assembly environment not only further induces superlattice transformations <sup>21–23</sup> but also produces orientational ordering of NCs within the superlattice. <sup>24–26</sup> In order to leverage the large top-down control and fabrication of such superlattices discovered from the bottom-up NC assembly, <sup>7,11,26</sup> it is apparently critical to gain an in-depth understanding of the structural correlations of such superlattice polymorphs and underlying kinetics <sup>27–31</sup> and further to construct a distinct roadmap of NC assembly from the early nucleation and growth of a metastable lattice through additional intermediate events to the final formation of a stable one. <sup>32–34</sup>

Instead of using spherical NCs that display structural simplicity and morphological uncertainty, we synthesize octahedral PbS NCs with well-controlled dimensions<sup>35</sup> as anisotropic building blocks to design the experiment, fabricate an environment cell, and develop the technique to investigate and analyze NC assembly (see the Experimental Section and the Supporting Information for full details). Such intelligent combination overcomes the limitations of previously studied samples of only several NC layers either with a fast nucleation rate or under a vacuum environment or both, enabling in situ and real time studies of NC assembly and subsequent growth at largely extended dimensions and under application-accessible operando conditions.

Through the systematic synchrotron-based in situ X-ray scattering experiments, we observed the spontaneous selfassembly of octahedral NCs into a NC-orientational disordered fcc 2D film and its subsequent transformation into a bcc superlattice with single NC-orientational ordering. Over the course of such a superlattice transformation, we discovered that this fcc-to-bcc solid-solid phase transformation did not undergo a deformation-based conventional martensitic transformation pathway and indeed involved an intermediate formation of a lamellar-confined liquid interface at the cost of the disassembly (melting) of fcc grains, which are smaller than a threshold grain size. Such an intermediate liquid represents another type of newly developed dense and disordered state of NCs, which recrystallize into an energyfavorable bcc phase. The recrystallization-based phase transformation was completed through the propagation of this intermediate liquid interface across the 2D fcc film. This condensed liquid-mediated phase transformation is associated with an energy reduction of 1.16  $k_BT$ , falling into the range of thermal fluctuation energy. With such a well-constructed kinetic roadmap and defined parameters, we further designed experiments to guide the superlattice nucleation and growth and successfully harvested the large and single bcc supercrystal with coherent ordering of NC translation and atomic plane orientation.

### **■ EXPERIMENTAL SECTION**

**Synthesis of Octahedral PbS NCs.** Octahedral PbS nanocrystals (NCs) were synthesized using a modified protocol. <sup>35</sup> Briefly, 0.87 g (2.3 mmol) of lead(II) acetate trihydrate and 3.5 mL (11 mmol) of oleic acid were mixed in 15 mL of diphenyl ether in a three-neck flask. The mixture in the flask was heated to 85 °C under a nitrogen atmosphere and thus degassed under vacuum ( $10^{-1}$  mbar) at 85 °C for 1.5 h. Subsequently, 50  $\mu$ L (0.87 mmol) of acetic acid was added to the solution under a nitrogen atmosphere and stirred for 10 min at 85 °C. The reaction solution was heated to 100 °C, and then, 1.0 mL (0.16 mmol) of the thioacetamide (TAA) solution was injected. The S precursor solution, called the TAA solution, was prepared by dissolving 0.16 g (2.2 mmol) of TAA in a mixture of 1.0 mL of *N*,*N*-

dimethylformamide and 12.0 mL of diphenyl ether and stored in a nitrogen filled glovebox. The reaction was quenched after 10 min by the removal of the heating mantle. To improve the quality of the synthesized NCs, 1.0 mL (13 mmol) of 1,2-dichloroethane was added together with acetic acid after the vacuum step. The resultant PbS NCs were purified with 5 mL of acetonitrile and centrifuged (4500 rpm, 5 min). After the removal of the supernatant, the collected NCs were resuspended in 2 mL of toluene. This process was repeated three times, and the harvested NCs were preserved in toluene for additional studies.

**Self-Assembly of Octahedral PbS NCs.** Octahedral PbS NCs were suspended in toluene with NC concentrations of 10 and 40 mg/mL, respectively. Such NC solutions were controlled under several designed environments for NC assembly.

Thin films of NC assembly were made using 10 mg/mL solutions of NCs in toluene. Typically,  $2{-}10~\mu$ L of the solution was drop-cast on substrates of Kapton tape, TEM grid, or silicon wafer under air conditions, and the evaporation took a minute or less.

2D NC assemblies with extended thicknesses were performed using a 40 mg/mL solution of NCs in toluene. Briefly, 2  $\mu$ L of the solution was injected into a glass capillary with 1 mm in diameter, and then, about 10  $\mu$ L of ethanol was quickly introduced into the capillary from another side. An air separating gap of  $\sim$ 1.5 cm was intentionally created in-between antisolvents of toluene and ethanol. Using soft wax, the two openings of the glass capillary were thoroughly sealed to form a close and stable environment. The antisolvents evaporate/diffuse at a considerately reduced rate, and the thick 2D assemblies were formed at the contact areas between glass wall and spreading solvents. The whole process took about 7 h.

3D NC assemblies at large scale were made using a 40 mg/mL solution of NCs in toluene controlled at a slow evaporation rate. About 300  $\mu$ L of the solution was stabilized in a small capped glass vial for NC assembly, and the whole process took about 2 weeks.

In Situ and Static Experimental Design and Characterization. Synchrotron-based small angle and wide-angle X-ray scattering (SAXS and WAXS) measurements were performed to characterize the NC assemblies under real time (in situ) and static environments at the  $B_1$  station of the CHESS, Cornell University. The monochromatic X-rays collimated at an energy of 25.514 keV were reduced to a 100  $\mu$ m diameter beam for the sample illumination. X-ray scattering patterns at small and wide angle ranges were collected using a large area Mar3450 detector. Both Ag-behenate and CeO<sub>2</sub> powder standards were used to calibrate the sample-to-detector distances and additional detector-seating parameters for SAXS and WAXS analysis, respectively.

Using the capillary-based environmental cell, the two sitting geometries of X-ray illumination on the solvent processing samples of in situ NC assembly inside the cell were designed and used in the real environmental measurements (Figure S2): (1) incident X-rays were foot-printed on the edge of the capillary and propagated tangentially across the inner capillary wall, called as *Tangential Incident SAXS* (TISAXS); (2) incident X-rays were delivered to illuminate directly through the central region of the glass capillary and penetrated through the capillary wall onto the NC assembly samples, called *Normal Incident SAXS* (NISAXS).<sup>37</sup> The TISAXS works in principle the same as that in the grazing incident SAXS (GISAXS), giving rise to similar X-ray scattering pattern, whereas the NISAXS originates from the in-plane X-ray scattering from the samples sitting on the inner capillary wall.

For the static experiments, NC assembled samples were loaded onto the Kapton tapes and then transferred onto the stage into the  $B_1$  station. A large area Mar3450 detector seated at an optimized distance from the sample was used to simultaneously collect both SAXS and WAXS images from the same volume of the samples.

Transmission electron microscopy (TEM) and scanning TEM (STEM) imaging, including high-angle annular dark field (HAADF) TEM imaging, were carried using a JEOL ARM 200 equipped with a probe corrector and an image corrector. Scanning electron microscopy (SEM) characterizations were performed on the NC assembly samples under various magnifications using a Hitachi

SU8010 operating at 5.0 kV. For individual NCs, the hexane-dispersed suspensions with a NC concentration of 10 mg/mL were dropped onto a carbon coating 200 mesh TEM copper grid and dried under air conditions. For the large, thick 2D and 3D NC assemblies, small fractions of superlattice crystals were taken and transferred with great caution from the capillary or glass vial onto the TEM grid or silicon substrate.

**Computation and Analysis.** A Fit2D program was used to reduce SAXS and WAXS images into 1D patterns with plots against two  $\theta$  (deg) or the inverse nanometer (nm<sup>-1</sup>). A CrystalMaker package was used to simulate and analyze the X-ray scattering and electron diffraction patterns for structural determination. Computer models of NC building blocks and assembled structures were constructed using packages of CrystalMaker, Vesta 3, and Cinema4d.

TISAXS and NISAXS patterns collected under in situ (real time) and static conditions were analyzed and indexed using a Matlab with a partial adaption and modification of the GIXSUI 1.6.2 package.<sup>38</sup> In a connection with the SAXS-indexed structure with the TIWAXS and NIWAXS patterns from the same volume of the sample, the orientational alignments of NCs in fcc and bcc are determined accordingly. A model of the rhcp structure was constructed on the basis of a mixed stacking sequence of ABCABC in fcc and ABABAB in hcp through a series of stacking faults, and then, the final rhcp stacking sequence was optimized to reproduce the X-ray scattering pattern as observed from the NC assembly.

Upon superlattice indexing, the X-ray scattering intensities and spotty distribution features of various superlattices were computed and modeled to define the total X-ray scattering loss and superlattice-based asymmetric offsets, full width at half maximums (fwhms) of inplane and out-of-plane scattering spots, and angular X-ray cross-correlation between various superlattices. Such data sets were fitted using various models to obtain parameters of superlattice domain size, growth rate, transformation interface width and propagation rate, Avrami exponent, and 2D film propagation rate. The details are given in the Supporting Information.

3D Structural Reconstruction at Reciprocal Space. A single supercrystal grain was loaded onto a mesh grid (MiTeGen) and transferred onto a homemade portable two-circle diffractometer to collect the full sets of SAXS and WAXS patterns using a large area detector (Mar3450). The sample was aligned with the rotation axis of Φ. Subsequently, both SAXS and WAXS images were collected upon rotation of the specimen from 0 to 180° at an angular interval of 1°. The full sets of SAXS and WAXS images were analyzed using Matlab to make the 3D structural reconstruction of the single supercrystal at the reciprocal space (see the Supporting Information for details). Briefly, the whole process was taken by converting the pixel index ( $x_p$ ,  $y_p$ ) $_{\Phi}$  of the detector at each rotation angle  $\Phi$  into the reciprocal space index  $(q_x, q_y, q_z)_0$ . Subsequently, the data sets were exported into a volumetric data visualization software, such as Avizo (Thermo Fisher Scientific) for visualization and analysis (see the Supporting Information for the details).

#### ■ RESULTS AND DISCUSSION

A typical TEM image (Figure 1a) reveals the great monodispersity of as-synthesized octahedral PbS NCs that have an average edge length of 10.5 nm (Figure 1b,c and Table S1). Synchrotron-based WAXS identifies that individual NCs have an atomic cubic rocksalt structure with a lattice constant of 5.946 Å (Figure 1d). Upon drop-casting of NC suspensions on a solid support, e.g., Kapton film, synchrotron-based SAXS characterizes the exclusive formation of a bcc superlattice that has a cell constant of 14.7 nm (Figure 1e). Individual domains of NC assembly controlled at a slow evaporation rate display a single orientational alignment of atomic crystallographic planes across the extensive array of NCs (Figures 1f,g and S1). 14

Controlled diffusion and evaporation of air-separated antisolvents (i.e., ethanol/toluene) with NC suspensions in a closely sealed glass capillary (Figures 2a and S2) dramatically

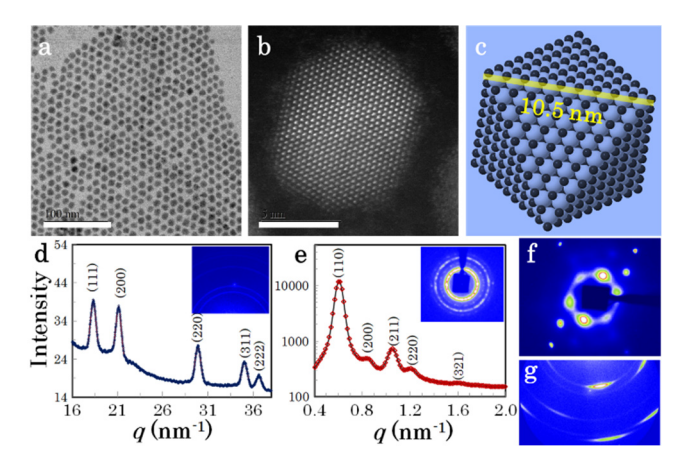
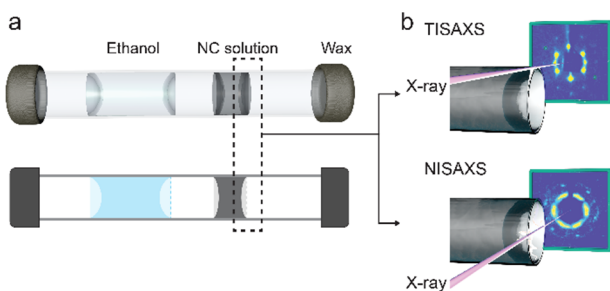


Figure 1. Structural characterizations of octahedral PbS nanocrystals (NCs): (a) transmission electron microscopy (TEM) image with (b) a high-angle annular dark field (HAADF) high resolution TEM image and (c) schematics of an octahedral PbS NC with surface terminations by eight PbS(111) facets. (d) Wide angle X-ray scattering (WAXS) pattern showing an atomic cubic rocksalt structure of individual NCs. (e) Small angle X-ray scattering (SAXS) pattern showing a body-centered cubic (bcc) superlattice of the NC assembly. (f) SAXS and (g) WAXS patterns collected from a single crystalline domain defined with the same orientation of (1.4 0.4 0.9) in an NC-assembled bcc superlattice and an atom-based cubic rocksalt lattice.

reduces the rate of NC assembly, allowing for the use of a synchrotron-based X-ray technique with accessible temporal and spatial resolutions to capture and identify the structural variation and underlying kinetics of the NC assembly under real solvent-processing environments. The two SAXS geometries at tangential and normal footprints of incident X-rays on the sample (Figure 2b) are designed to make complementary collections of both in-plane and out-of-plane structural information, capable of not only an overall structural reconstruction of NC assembly but also a quantitative determination of the kinetic rates of the underlying events, i.e., superlattice nucleation, growth, transformation, and so on.

Figure 2c presents several typical tangential and normal incident SAXS (TISAXS and NISAXS) patterns of octahedral PbS NC assemblies collected under real solvent processing environments of 40 mg/mL NC concentrations (Videos S1 and S2 for complete data sets). The observed variation of in situ SAXS as a function of time reveals the four key stages of NC assembly (Figure 2c and Table 1), including (1) early nucleation of unbound molecules on the front-spreading solvent surfaces, (2) nucleation and growth of the fcc superlattice, (3) fcc-to-bcc solid—solid phase transformation, and (4) subsequent condensation of the final bcc superlattice. Over the early solvent processing period of ~417 min, NC assembly also involves additional events (Table 1), which include rich and subtle kinetic details.

**Preliminary Nucleation Event.** At the very early stage, NC suspensions undergo a primary ordering event of oleic acid (OA)-based unbound molecules on the solvent surfaces. A typical TISAXS pattern (Figure 2c at 0 min) displays a series of parallel arc-shape spots, in which one guiding line through a connection of parallel spots with a defined symmetric center deviates from the vertical dimension at an angle of  $10^{\circ}$  (Figure S3). These X-ray scattering spots develop a positional correlation of  $q_i/q_1 = 1:2:3$ , indicative of the formation of a lamellar structure with an interlayer spacing of 5.06 nm, equivalent to the molecular length of lead oleates [Pb(OA)<sub>2</sub>]



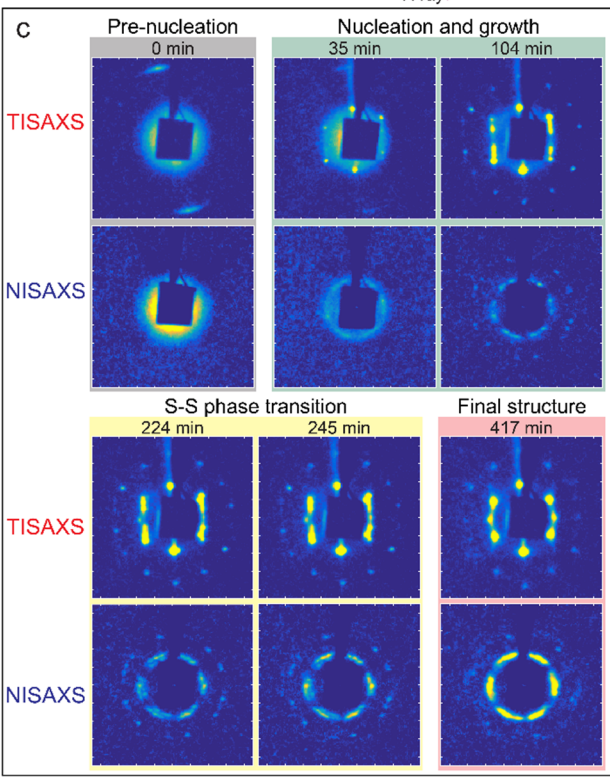


Figure 2. Experimental setup and typical tangential and normal incident SAXS (TISAXS and NISAXS) patterns collected in situ from the NC assembly under real solvent processing conditions: (a) capillary-based environment cell of the NC assembly in the view of a 3D (top) and 2D (bottom) cross-section; (b) experimental schematics of in situ TISAXS (top) and NISAXS (bottom) geometries.; (c) typical TISAXS and (d) NISAXS patterns collected under real solvent processing environments, identifying the four dominant stages of the NC assembly: (1) prenucleation of lamellar molecules; (2) nucleation and growth of the fcc superlattice; (3) fcc-to-bcc solid—solid phase transition; (4) final bcc superlattice. Note: fcc and bcc represent face-centered cubic and body-centered cubic superlattices, respectively.

under solvent-wetting environments (Figures 3 and S4 and Table S2). Apparently, these OA-based molecules are initially bonded with Pb atoms and subsequently detached from NC surfaces as a molecular form of  $[Pb(OA)_2]$  into nonpolar solvents, e.g., toluene (Table S2). The resultant ordering layers are seated on the tilting surfaces of spreading solvents on the inner capillary wall. The wetting state developed at a starting tilt angle  $(\theta)$  of  $10^\circ$  represents an equilibrium achieved between the wetting solvent liquid (L) on the solid capillary wall (S) in a vapor phase (V) through the Young equation, which is written as

Table 1. Experimentally Observed and Determined Parameters of Octahedral PbS NC Assembly at Various Stages<sup>a</sup>

	molecular ordering	the fcc nucleation and growth	the fcc-to-bcc transformation	densification of single bcc
starting/ ending time (min)	0/18	18/160	160/320	320/417
total time (min)	18	142	160	97
propagation rate $(\mu m/min)$	extremely quick	1.23	0.74	0.74
interface width $(\mu m)$			18.5	

"Note: After the solvent processing time of 417 min, the resultant single bcc remains stable in both structure and volume.

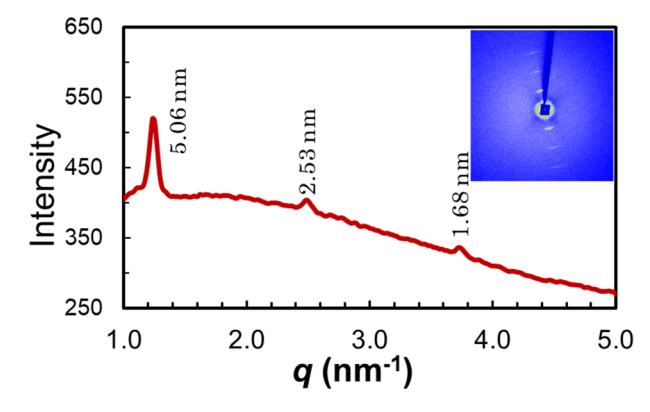


**Figure 3.** Synchrotron-based X-ray scattering pattern of OA-based molecular ordering observed on the front-spreading solvent surfaces at the very early stage of NC assembly.

$$\cos \theta = \frac{\gamma_{\rm SV} - \gamma_{\rm SL}}{\gamma_{\rm LV}} \tag{1}$$

where  $\gamma$  represents the surface energy of a given interface at equilibrium.

As the antisolvents proceed gradually with both diffusion and evaporation at a slow rate, the spreading frontline of the NC suspending solvent recesses, and accordingly, the [Pb-(OA)<sub>2</sub>] lamellar layers reduce in tilt angle. As shown in Figure S5, upon reduction of the front solvent tilt angle during the solvent-evaporation process, the surface tensions at the triple interfaces induce gradual enhancement of the driving (solvent contraction) forces in both directions, which are perpendicular and parallel to the solid capillary wall, respectively. This process accordingly triggers the nucleation and growth of the NC assembly and additional intermediate events (Figure 2c).

**Nucleation and Growth of Metastable fcc Superlattice.** As the solvent surface reduces its tilt angle to  $4^{\circ}$  (t = 18 min), the X-ray scattering intensity of lamellar  $Pb(OA)_2$  ordering layers is dramatically weakened, and an additional set of X-ray scattering spots appear accordingly (Figures 2c at 35 min; S3b), indicative of the nucleation of a fcc superlattice. As the exponent of n = 2.2 is derived from an Avrami analysis on the growing superlattice crystals (Figure S6),  $^{40}$  the fcc phase is favored by a 2D growth of nucleated grains on the solid capillary wall, which coincidently develop a single fcc(111) out-of-plane orientation (Figure 2c at 35 min; Figure 4a-e) and random fcc(110)-preferred in-plane orientations (Figure

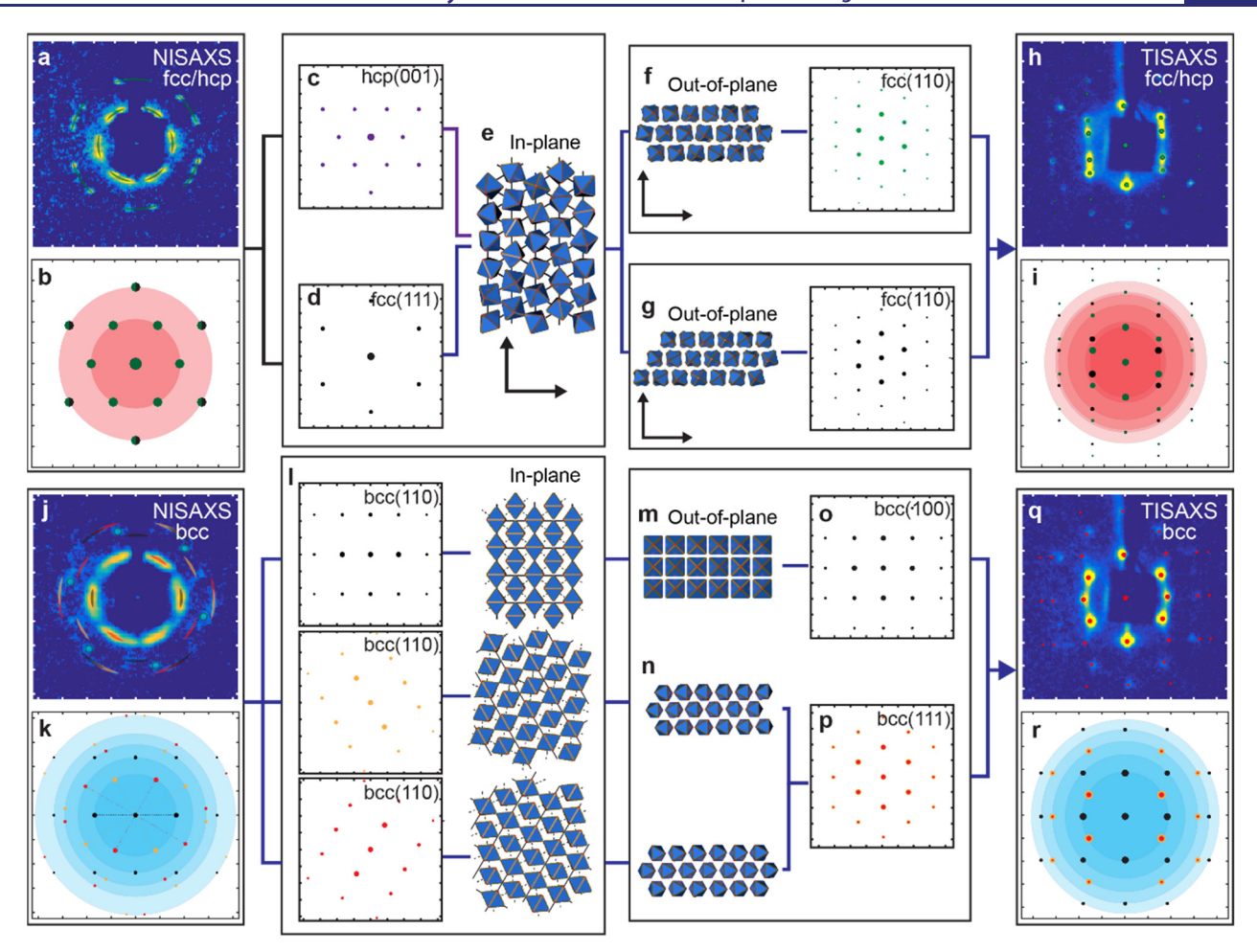


Figure 4. NISAXS and TISAXS patterns of fcc/hcp and bcc superlattices: (a-i) Structural analysis of fcc and hcp through a correlation and connection between TISAXS and NISAXS observations. (j-r) Structural analysis and correlation of bcc between TISAXS and NISAXS observations. For the NISAXS patterns of fcc/hcp (a) and bcc (j) and corresponding theoretical patterns (b, k), each one decomposes into individual domains of fcc/hcp (c-e) and bcc (l), whereas each computed TISAXS pattern of fcc (f, g) and bcc (m-p) is merged to compare with the experiments (h, i; q, r). Similarly, the TISAXS patterns are also analyzed as fcc (f, g) and bcc (o, p) with merged patterns (i, r) of each computed one. Note: The hcp-based TISAXS analysis can be found in Figure S8.

2c at 35 min; Figure 4f–i). Upon 2D growth of fcc grains as indicated by a dramatic enhancement of spotty intensity, the 2D fcc grains collectively develop a twinning-like in-plane structure, in which the two sets of fcc(110)-preferred grains are arranged in order, sharing a fcc(112)-directed interface (Figure 2c at 104 min; Figure 4f–i). The development of such a twinning-like in-plane structure implies a growth-induced attachment and rearrangement of fcc grains through boundary interactions, which transform the aggregated fcc grains into a largely extended 2D superlattice film with substantial improvement of in-plane fcc(110) ordering texture (Figure 2c at 104 min).

Individual fcc grains display an anisotropic supercrystal growth, in which the growth rates of individual grains within in-plane and out-of-plane are determined to be 14 and 3 nm/min, respectively (Figure S7). The overall 2D superlattice film propagates across the capillary wall at a rate of 1.23  $\mu$ m/min (Table 1). At t=130 min, the 2D fcc grains reach the maximum of domain size (e.g.,  $\sim$ 840 nm). The fcc growth does not show apparent Oswald ripening (Figure 2c at 34 and 104 min: NISAXS) but involves a noticeable development of stacking faults (Figure 2c at 104 min: TISAXS), so that a random hexagonal close packing (rhcp) lattice sporadically

appears in the film (Figure S8). Additional computation determines the rhcp stacking sequence of ABCBABCABCAC (Figure S8e,f), which represents an intermediately mixing sequence of fcc (ABCABC) and hcp (ABABAB) (Figure S8g). The 6-fold symmetry of the X-ray scattering spots observed in both fcc and rhcp (Figure 4a,b) reveals the crystallographic correlations of in-plane fcc(220)//rhcp(110) and out-of-plane fcc(111)//rhcp(001) (Figure 4c,d).

Solid–Solid Phase Transformation from fcc to bcc Superlattice. As the evaporation-induced solvent recession moves forward, additional X-ray scattering spots emerge at  $t=160\,$  min (Table 1) and are accordingly indexed as a bcc superlattice, indicative of a fcc-to-bcc solid—solid phase transformation (Figure 2c at 224 min). The bcc coexists with fcc over a superlattice growth course of 160 min, and at  $t=320\,$  min, a single bcc phase is completely formed (Table 1). This single bcc phase reduces its volume until  $t=417\,$  min (Figure S10) and then remains stable in both structure and volume (Figure 2c at 417 min, Videos S1 and S2).

Over the coexisting range of the two superlattice polymorphs (Figure 2c at 224 and 245 min), the bcc(110) consistently overlaps in the X-ray scattering spotty position with the fcc(111) in out-of-plane, but within in-plane, the

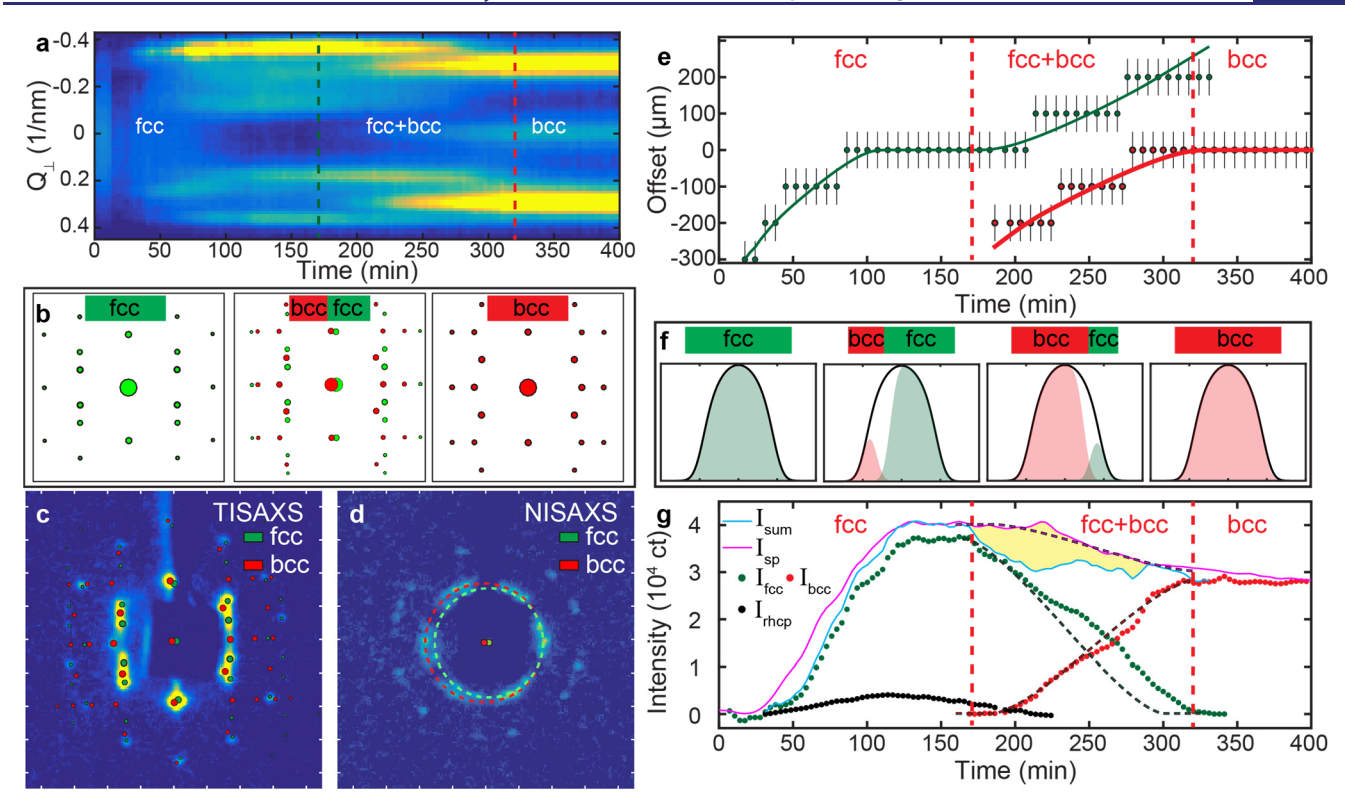


Figure 5. Liquid interface mediated fcc-to-bcc superlattice phase transformation: (a) integrated intensity of the selected TISAXS region (see Figure S17a) against the wave vector ( $Q_{\perp}$ , vertical component) and time. (b) Demonstration of the scattering asymmetric scattering offset of fcc and bcc with various ratios within the interface region. (c, d) Observed offsets in (c) TISAXS and (d) NISAXS patterns. (e) Variation of the observed offset as a function of time. (f) Intensity distribution of fcc and bcc and their ratio within the interface region upon the transformation processing. (g) Total X-ray scattering variations of various superlattices as a function of time, in which the shallow area in yellow highlights the loss of total X-ray scattering within in-plane, indicative of the existence of a liquid-like phase behind phase transformation.

bcc(110) becomes smaller in spacing than fcc(111) (Figure S10). Such observations indicate a significant discontinuity of in-plane NC packing but a continuous presence of the original lamellar geometry of out-of-plane NCs. Upon accomplishment of the phase transformation, all the bcc domains develop with a single bcc(110) out-of-plane orientation (Figures 4q,r and S11), which seemingly inherits the 6-fold spotty symmetry (Figure 4j,k) from the fcc domains (Figure 4a,b). In principle, each single bcc(110)-oriented domain produces only one pair of symmetric bcc(110) spots (Figures 4l and S12). Therefore, the observed 6-fold symmetric spots stem indeed from at least the three sets of bcc(110) in-plane domains, which are arranged into order at an angular separation of 120° (Figure 4k,l). As the three sets of in-plane bcc grains are examined in the out-of-plane direction, one set has the bcc(100) orientation (Figure 4m,o), whereas the other two sets hold identical bcc(111) orientations (Figure 4n,p). A structural projection of three individual domains into one single SAXS pattern agrees with the experimental observations (Figure 4q), well explaining the orientation-induced loss of certain X-ray scattering spots (Figures 4h,i,q,r and S11-S13).

Hidden Lamellar-Confined NC Liquid Behind Phase Transformation. The fcc-to-bcc solid—solid phase transformation takes place as a consequence of the solvent evaporation-induced thermodynamic and kinetic processes so that the energy difference between the two superlattices is only on the order of thermal fluctuation energy, i.e., several  $k_{\rm B}T$  (Figure S5). Synchrotron-based WAXS characterization reveals an additional orientational transformation of NCs from the random orientations in fcc to a single orientational ordering in

bcc (Figure S14). In a comparison of TEM-defined NC dimensions (i.e., the tip-to-tip length = 14.85 nm and the edge length = 10.5 nm) with SAXS-determined inter-NC distance of 14.08 nm and inter-NC separating gap of 4.03 nm in fcc at the transition stage, no sufficient free space allows NCs to rotate or diffuse directly from the random orientations in fcc into a single orientation to form the bcc phase (Figure S15a). Obviously, both energy and space are not satisfied to induce either a deformation-driven or a diffusion-based fcc-to-bcc solid—solid phase transformation (Figure S15 and Video S3).

Alternatively, this fcc-to-bcc solid-solid phase transformation is mediated through an unconventional and hidden intermediate liquid state (Figure 5). At the interface-mediated region where both fcc and bcc coexist (Figure 5a) but are separate by an interface (Figure 2c at 224 and 245 min), either phase of bcc and fcc develops a noticeable asymmetric distribution of X-ray scattering spots over the course of phase transformation. Accordingly, an offset appears between the two defined virtual centers: (1) symmetric center of superlatticebased X-ray scattering spots and (2) static center of incident Xray window (Figure S16). If the phase transformation takes place in random sites or grains of the early nucleated fcc superlattices, the offset should be zero. However, at the early stage of either the superlattice nucleation or the phase transformation, fcc and bcc always start with an asymmetric offset, in which the static center of the X-ray window does not overlap with the defined center by the superlattice-scattered Xray spots (Figures 5b-d and S17 and S18). Upon superlattice growth, the resultant 2D film propagates across the X-ray window, and accordingly, the two virtual centers approach so

that the resultant offset displays gradual variations as functions of time and intensity as a consequence of increased/decreased ratios of fcc/bcc across the static X-ray window (Figure 5e).

Once the phase transformation takes place, the interface-mediated region enters into and propagates across the X-ray window (i.e.,  $100~\mu m$  in diameter) (Figure S19), producing a reliable correlating variation of the fcc/bcc ratio as a function of time (Figure 5e). The observed variation of time-dependent offset reveals a transition-induced increase of the bcc phase and a simultaneous decrease of the fcc phase as well as the ultimate formation of a single bcc phase across the entire X-ray window (Figure 5b,e). On the basis of such time-dependent offset variations of both fcc and bcc phases (Figures 5e,f and S20), the propagation rate of the interface across the capillary wall is determined to be  $0.74~\mu m/min$ . Equivalently, the bcc phase also has a propagation rate of  $0.74~\mu m/min$ , smaller than the fcc one of  $1.23~\mu m/min$  (Table 1).

A profile analysis and correlation of the total X-ray scattering intensities between various superlattices as a function of time further reveal a significant loss of in-plane total X-ray scattering intensity, but a consistency of out-of-plane specular scattering intensity cross the interface-mediated region (Figures 5g, S17d-h, and S21). In a conjunction with the observed structural features under the interface-mediated region (Figures 5a and 6a and Table 1), a liquid state of NC disorder

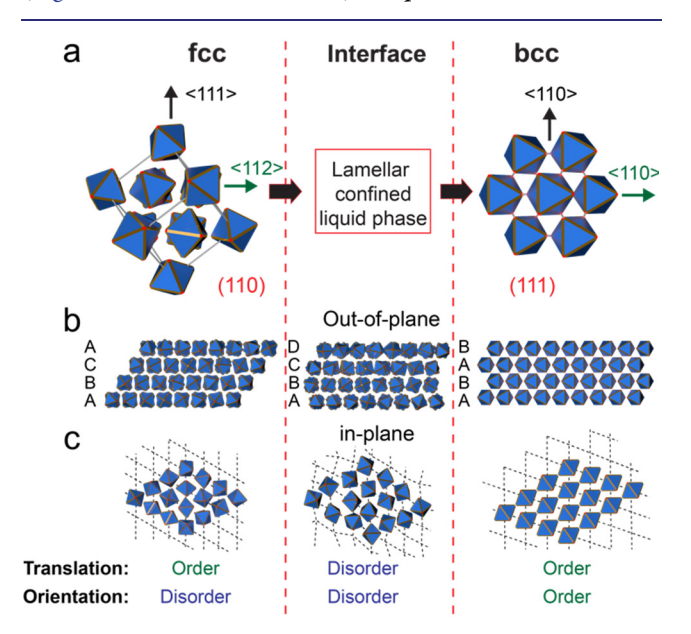


**Figure 6.** Schematic illustration of the fcc-to-bcc solid—solid phase transformation mediated by a lamellar-confined liquid interface: (a) cartoon demonstration of superlattice orientations between fcc and bcc as separated by a lamellar confined NC liquid interface; (b) out-of-plane and (c) in-plane schematic views of NC arrangements in fcc and liquid and bcc phases. Note: the ABCD in (b) shows that all the layers do not have a defined periodically stacking sequence, and the dotted lines in (c) are a guide to see the translational (or positional) order of the NCs within in-plane.

does exist within lamellar in-plane layers (Figures 6b,c and S17d-g), attributed to the observed partial loss of the total in-plane X-ray scattering intensity and the structural discontinuity of in-plane NC arrangements (Figure 6c). In addition, the lamellar-like structure continuously remains throughout, maintaining the consistence of the total out-of-plane X-ray scattering intensity over the course of the fcc-to-bcc phase

transformation (Figure 6b). A fit of the X-ray scattering intensities with the lost ratio to that of both fcc and bcc within the X-ray window gives rise to a liquid interface width of 18.5  $\mu$ m (Figure 5g). A total scattering computation of the lamellar confined liquid interface model with a coexistence of fcc and bcc superlattices in the X-ray window well reproduces the experimental observations. A time-dependent lagging effect is also identified in fcc, reasonably explaining the preferred preservation of the large fcc domains without an intermediate NC disassembly in the film (Figures S9 and S21).

When it is assumed that a critical domain size is associated with the superlattice growth, the fcc grains are mostly smaller than the critical size as claimed previously in the classic theory of crystal growth. These small fcc grains become unstable and thus disassemble into a disordered NC liquid. As a consequence, a stable bcc phase recrystallizes from such a highly condensed liquid and continues to grow large (Figures 5g and S7b). Unlike the classic crystal growth model that describes the continuous growth of large grains at a cost of small ones,  $^{1-3}$  the NC liquid from the disassembly of small metastable fcc grains is confined in a lamellar environment and recrystallizes into an energy-favorable bcc phase, rather than promoting a continuous growth of the large fcc domains, e.g., the experimentally defined size of 1.4  $\mu$ m (Figure S9, strong spots as highlighted in the circle) on average.

Solution calorimetric measurements of NC disassembly in a nonpolar solvent reveal a slight energy difference of NC assemblies between bcc and fcc. The octahedral PbS NCs undergo a similar solvent-based NC assembly and disassembly consequence, so that the reduced energy in the bcc relative to the fcc polymorph is estimated by the magnitude of  $\sim 1.16~k_{\rm B}T$  (Table S3 and Figure S24), falling into the range of the thermal fluctuation energy in the solvent-based spontaneous process of NC assembly (Figure S5).

An apparent relation of epitaxial orientations exists between fcc and bcc (Figure 4a,j). Besides the observed inherence of the 6-fold symmetric feature of the X-ray scattering spots, each individual spot is indeed composed of the three sub ones (Figure S22a), which develop an angular difference of ±5° between fcc and bcc. An angular X-ray cross-correlation analysis (AXCCA) (Figure S22b,c) gives rise to a well-defined correlation of  $60^{\circ} \times n - 5^{\circ}$  (n = integer) between the six dominant peaks. When the bcc(110)-based 2D in-plane lattice (Figure S22d) as a deformed 2D hexagon from the fcc(111) is taken into account, the angular rotation  $(\varphi)$  of  $\pm 5^{\circ}$  is very close to the orientational difference of 5.26° between fcc(111) and bcc(110) (Figure S22e,f). The three sets of fcc(111) and bcc(110) in-plane grains arrange themselves in order but leave a total volumetric void of ~8.3% (Figure S23a), which provides additional in-plane freedom for the rotation of disordered NCs into a single orientational ordering to form the bcc superlattice. While the observed cracks in the dry bcc film (Figure S23b) reveal the in-plane anisotropic strength and the existence of additional space as required for the orientational transformation of NCs through an in-plane NC rotation (Figure 6c), the peak broadening of bcc and resultant reduction of the calculated domain size (Figure S7) indicates the occurrence and residue of large strains across the superlattice film.

Scalable Fabrication of Large and Single bcc Supercrystal by Design. Directed by such an in situ constructed kinetic roadmap of octahedral NC assembly, we design experiments with the use of highly concentrated NC

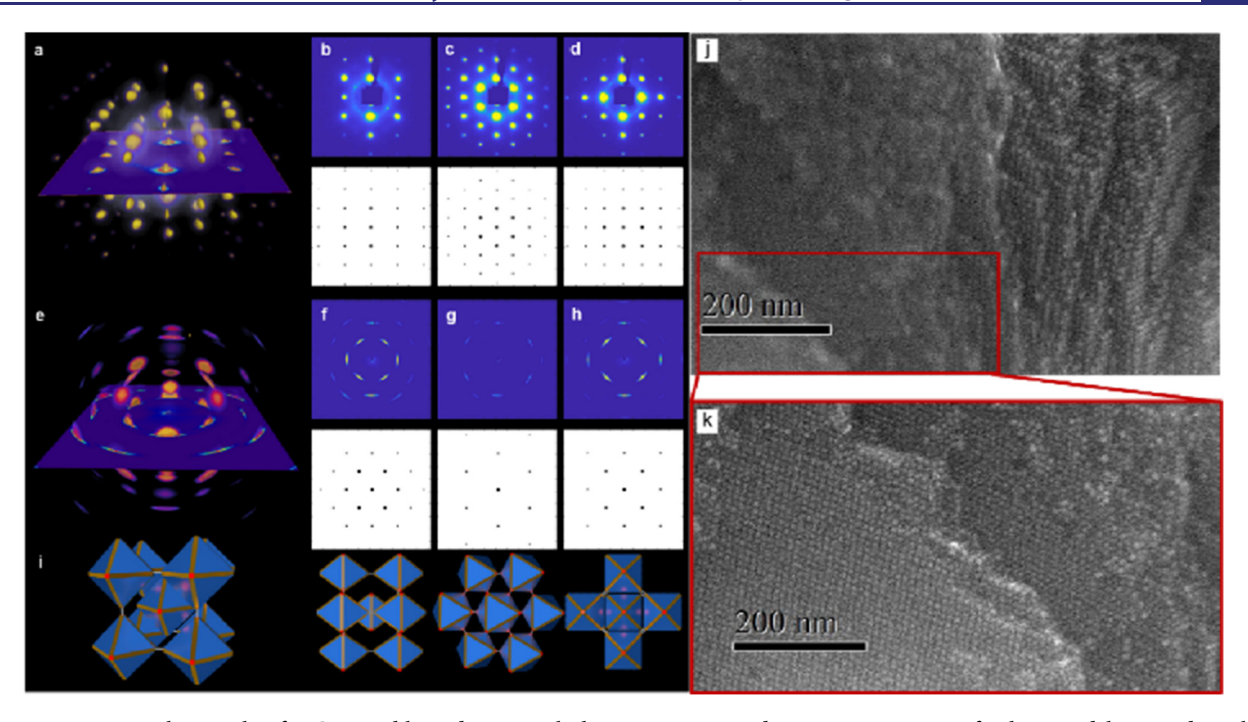


Figure 7. Experimental controls of NC assembly and structural characterizations and 3D reconstruction of a harvested large and single 3D supercrystal from the designed experiments: (a) 3D superlattice reconstruction of the bcc supercrystal at reciprocal space with (b-d, top) experimental and (b-d, bottom) computational SAXS patterns at projections of (b) SL(110), (c) SL(111), and (d) SL(100), respectively. (e) 3D atomic structural reconstruction of cubic rocksalt PbS NCs at reciprocal space with (f-h, top) experimental and (f-h, bottom) computational WAXS patterns at projections of (f) PbS(110), (g) PbS(111), and (h) PbS(100), respectively. (i) Cartoon demonstration of the derived bcc superlattice with NC orientations from (a-h). (j, k) Typical high-angle annular dark field (HAADF) TEM images of the harvested large bcc supercrystal with a focus of the electron beam into various depths.

suspensions in a single nonpolar solvent (e.g., toluene) and controlled at a slow evaporation rate to exclusively fabricate the single and largely extended supercrystal with fully ordering coherences of NC translation in bcc and atomic crystallographic orientation across NC arrays. NC suspensions in a starting solution with a high concentration undergo a crystallization process of bcc superlattice similar to that which takes place in the fcc-disassembled high density NC liquid, excluding the inherent preservation of the twinning and stacking faults from the early nucleated multiple fcc/rhcp grains under a low NC concentration environment (Figure S13 and Video S4).<sup>34</sup> A slow evaporation of single nonpolar solvent continues to condense NCs homogeneously in solution, avoiding the gradient development of antisolvent-diffusion induced NC concentration<sup>43</sup> and further overcoming the local nucleation of random free-standing bcc grains, formation of thin and multiple-grained films, and structural discontinuity of supercrystals across domains. When the key constraints above are taken into account, scalable fabrication of the desired single bcc supercrystal can be achieved using a single solvent processing of highly concentrated NCs. However, a large container is required to weaken or eliminate the curvatureinduced capillary effect.

3D structural reconstructions of the harvested large supercrystal at the reciprocal space<sup>44</sup> with a combination of experimental and computational X-ray scattering patterns at both the SAXS and WAXS ranges (Figure 7a-h and Videos S5-S8) evidently reveal the fully ordering coherences of NC translation in the bcc symmetry and atomic crystallographic plane orientation across the entire specimen (Figure 7i). Both NC assembly in bcc superlattice and constituent PbS NCs in atomic cubic rocksalt (RS) lattice develop the structural

correlations of  $SL(111)_{bcc}//PbS(111)_{RS}$ ,  $SL(110)_{bcc}//PbS(110)_{RS}$ , and  $SL(100)_{bcc}//PbS(100)_{RS}$ . The constituent building blocks of octahedral NCs arrange themselves in bcc with perfect alignments of vertex-to-vertex and face-to-face in the SL[100] and SL[111] directions, respectively (Figure 7i). High-angle annular dark field (HAADF) TEM images further confirm the single crystallinity of the large bcc supercrystal (Figure 7j,k).

### CONCLUSIONS

In situ and static synchrotron-based X-ray scattering experiments, supported by calculations of the total X-ray scattering and observed offset with an overall analysis of energy and space and NC crystallographic orientation, allow one to fully construct the kinetic roadmap of octahedral PbS NC assembly from the early nucleation and growth of metastable fcc through a liquid-mediated solid-solid phase transformation to the final formation of the stable bcc superlattice. The NC assembly starts with a primary ordering of unbound Pb(OA)<sub>2</sub> molecules on the front-spreading solvent surfaces. As the antisolvents evaporate and diffuse at a slow rate, NC solubility reduces in solvents, and accordingly, the thermodynamic and kinetic states of NC solutions are developed to change the surface tension strength at the solvent/substrate/air interfaces. While the solvent surface reduces in tilt angle to 4°, the enhanced directional forces drive octahedral NC self-assembly into an orientationally disordered fcc superlattice. As the fcc grains grow and aggregate, they become unstable and disassemble into NC-disordered liquids, which are confined under a lamellar environment. Consequently, the stable bcc phase crystallizes from such highly concentrated NC liquids and displays a single orientational ordering of NCs at a reduced

free energy of 1.16  $k_BT$ . The dominant interactions between NC-coated molecules control the early fcc nucleation from the dilute NC solution, whereas the enhanced directional entropic forces from shaped NC cores guide the late bcc crystallization from the disassembly developed dense NC liquid. With such a defined parameter and gained insights, designable control and scalable fabrication is achieved to harvest the large and single bcc supercrystal with fully ordering coherence of both NC translation and atomically crystallographic orientation. The constructed kinetic NC assembly roadmap and defined parameters of superlattice growth and film propagation provide a solid foundation for controlled design and scalable fabrication of the desired large supercrystals, whereas the discovered lamellar-confined NC liquid interface behind solid-solid phase transformation sheds new light on the physics of the crystal nucleation and growth of materials at both the atomic and mesoscale levels.

#### ASSOCIATED CONTENT

# **Solution** Supporting Information

The Supporting Information is available free of charge at https://pubs.acs.org/doi/10.1021/jacs.0c12087.

Additional data sets include figures, tables, detailed analysis on in situ TISAXS and NISAXS patterns, rhcp analysis, computational model for interface-mediated phase transformation, and 3D reconstructions at reciprocal space (PDF)

Video S1: in situ TISAXS patterns collected from the octahedral PbS NC assembly, in which NC suspensions have a concentration of 40 mg/mL in toluene (AVI)

Video S2: in situ NISAXS patterns (AVI)

Video S3: variation of computed TISAXS patterns (AVI)

Video S4: in situ TISAXS patterns collected from the octahedral PbS NC assembly, in which NC suspensions have a concentration of 10 mg/mL in toluene (AVI)

Video S5: variation of single supercrystal SAXS image (AVI)

Video S6: 3D structural reconstruction of single supercrystal at the reciprocal space based on the SAXS datasets (MPG)

Video S7: variation of single supercrystal WAXS image (AVI)

Video S8: 3D structural reconstruction of single supercrystal at the reciprocal space based on the full sets of WAXS images (MPG)

#### AUTHOR INFORMATION

# **Corresponding Author**

Zhongwu Wang — Cornell High Energy Synchrotron Source, Cornell University, Ithaca, New York 14853, United States; orcid.org/0000-0001-9742-5213; Email: zw42@ cornell.edu

#### **Authors**

Xin Huang — Cornell High Energy Synchrotron Source, Cornell University, Ithaca, New York 14853, United States; oorcid.org/0000-0001-5404-4437

Jinlong Zhu – Department of Physics, South University of Science and Technology, Shenzhen, Guangdong 518055, China Binghui Ge – Key Laboratory of Structure and Functional Regulation of Hybrid Materials of Ministry of Education, Institutes of Physical Science and Information Technology, Anhui University, Hefei, Anhui 230601, China

Frauke Gerdes – Institute of Physical Chemistry, University of Hamburg, 20146 Hamburg, Germany

Christian Klinke — Institute of Physics, University of Rostock, 18059 Rostock, Germany; Department of Chemistry, Swansea University, Swansea SA2 8PP, Uunited Kingdom; orcid.org/0000-0001-8558-7389

Complete contact information is available at: https://pubs.acs.org/10.1021/jacs.0c12087

#### Notes

The authors declare no competing financial interest.

#### ACKNOWLEDGMENTS

We appreciate technical support of all the CHESS staff and scientific discussion with many colleagues across the Cornell campus and at other institutions. Special thank goes to Dr. Ruipeng Li for his technical assistance at the early stage. The CHESS is supported by the NSF awards DMR-1332208 and DMR-1829070. X.H. is partially support by the Center for Alkaline-Based Energy Solutions (CABES), funded by the U.S. Department of Energy under Award No. DE-SC0019445. This work made use of the Cornell Center for Materials Research Shared Facilities, which are supported through the NSF MRSEC program (DMR-1719875).

#### REFERENCES

ı

- (1) Ostwald, W. Studien über die Bildung und Umwandlung fester Körper. 1. Abhandlung: Übersättigung und Überkaltung. *Z. Phys. Chem.* **1897**, 22, 19.
- (2) Abraham, F. F. Homogeneous nucleation theory; Academic Press: New York, 1974.
- (3) De Yoreo, J. J.; Vekilov, P. G. Principles of crystal nucleation and growth. *Rev. Mineral. Geochem.* **2003**, *54*, 57–93.
- (4) Zheng, H. M.; et al. Obervation of single colloidal platinum nanocrystal growth trajectories. *Science* **2009**, *324*, 1309–1312.
- (5) De Yoreo, J. J.; SommerdijK, N. A. J. M. Investigting materials formation with liquid-phase and cryogenic TEM. *Nat. Rev. Mater.* **2016**, *1*, 16035.
- (6) Wu, S.; Li, M.; Sun, Y. In situ synchrotron X-ray characterization shining light on the nucleation and growth kinetics of colloidal nanoparticles. *Angew. Chem., Int. Ed.* **2019**, *58*, 8987–8995.
- (7) Boles, M. A.; Engel, M.; Talapin, D. V. Self-assembly of colloidal nanocrystals: from intricate structures to functional materials. *Chem. Rev.* **2016**. *116*. 11220–11289.
- (8) Huang, X.; Wang, Z. Supercrystallography-based decoding of structure and driving force of nanocrystal assembly. *Materials* **2019**, 12 (22), 3771.
- (9) Li, T.; Senesi, A. J.; Lee, B. Small angle X-ray scattering for nanoparticle research. *Chem. Rev.* 2016, 116, 11128–11180.
- (10) Damasceno, P. F.; Engel, M.; Glotzer, S. C. Predictive self-assembly of polyhedra into complex structures. *Science* **2012**, 337, 453–457.
- (11) Deng, K.; Luo, Z.; Tan, L.; Quan, Z. Self-assembly of anisotropic nanoparticles into functional superstructures. *Chem. Soc. Rev.* **2020**, *49*, 6002–6038.
- (12) Henzie, J.; Grunwald, M.; Widmer-Cooper, A.; Geissler, P. L.; Yang, P. Self-assembly of uniform polyhedral silver nanocrystals into densest packings and exotic superlattices. *Nat. Mater.* **2012**, *11*, 131–137.

- (13) Murray, C. B.; Kagan, C. R.; Bawendi, M. G. Synthesis and characterization of monodisperse nanocrystals and close packed nanocrystal assemblies. *Annu. Rev. Mater. Sci.* **2000**, *30*, 545–610.
- (14) Li, R.; Zhang, J.; Tan, R.; Gerdes, F.; Luo, Z.; Xu, H.; Hollingsworth, J. A.; Klinke, C.; Chen, O.; Wang, Z. Competing interactions between various entropic forces toward assembly of  $Pt_3Ni$  octahedra into a body-centered cubic superlattice. *Nano Lett.* **2016**, 16, 2792-2799.
- (15) Liu, W.; Tagawa, M.; Xin, H. L.; Wang, T.; Emamy, H.; Li, H.; Yager, K. G.; Starr, F. W.; Tkachenko, A. V.; Gang, O. Diamond family of nanoparticle superlattices. *Science* **2016**, *351*, 582–586.
- (16) Lin, H. X.; et al. Clathrate colloidal crystals. Science 2017, 355, 931-935.
- (17) Nagaoka, Y.; Tan, R.; Li, R.; Zhu, H.; Eggert, D.; Wu, Y. A.; Liu, Y.; Wang, Z.; Chen, O. Superstructures generated from truncated tetrahedral quantum dots. *Nature* **2018**, *561*, 378–382.
- (18) Senyuk, B.; et al. Topological Colloids. *Nature* **2013**, 493, 200–205.
- (19) Ye, X.; Chen, J.; Irrgang, M. E.; Engel, M.; Dong, A.; Glotzer, S. C.; Murray, C. B. Quasicstalline nanocrystal superlattice with partial matching rules. *Nat. Mater.* **2017**, *16*, 214–219.
- (20) Nagaoka, Y.; Zhu, H.; Eggert, D.; Chen, O. Single-component quasicrystalline nanocrystal superlattices through flexible polygon tiling rule. *Science* **2018**, *362*, 1396–1400.
- (21) Zhang, Y.; Pal, S.; Vo, T.; Kumar, S.; Gang, O. Selective transformation between nanoparticle superlattices via the reprogramming of DNA-mediated interactions. *Nat. Mater.* **2015**, *14*, 840–847.
- (22) Schmitt, J.; Hajiw, S.; Lecchi, A.; Degrouard, J.; Salonen, A.; Imperor-Clerc, M.; Pansu, B. Formation of superlattices of gold nanoparticles using Ostwald ripening in emulsions: transition from fcc to bcc structure. *J. Phys. Chem. B* **2016**, *120*, 5759–5766.
- (23) Wang, Z.; Schliehe, C.; Bian, K.; Dale, D.; Bassett, W. A.; Hanrath, T.; Klinke, C.; Weller, H. Correlating superlattice polymorphs to internanoparticle distance, packing density and surface lattice in assemblies of PbS nanoparticles. *Nano Lett.* **2013**, *13*, 1303–1311.
- (24) O'Brien, M. N.; Girard, M.; Lin, H. X.; Millan, J. A.; Olvera de la Cruz, M.; Lee, B.; Mirkin, C. A. Exploring the zone of anisotropy and broken symmetries in DNA-mediated nanoparticle crystallization. *Proc. Natl. Acad. Sci. U. S. A.* **2016**, *113*, 10485–10490.
- (25) Lu, F.; Vo, T.; Zhang, Y.; Frenkel, A.; Yager, K. G.; Kumar, S.; Gang, O. Unusual packing of soft-shelled nanocubes. *Science Advances* **2019**, *5*, eaaw2399.
- (26) Li, R.; Bian, K.; Hanrath, T.; Bassett, W. A.; Wang, Z. Decoding the superlattice and interface structure of truncate PbS nanocrystal assembled supercrystal and associated interaction forces. *J. Am. Chem. Soc.* **2014**, *136*, 12047–12055.
- (27) Weidman, M. C.; Smilgies, D. M.; Tisdale, W. A. Kinetics of the self-assembly of nanocrystal superlattices measured by real-time in situ x-ray scattering. *Nat. Mater.* **2016**, *15*, 775–781.
- (28) Geuchies, J. J.; et al. In situ study of the formation mechanism of two dimensional superlattices form PbSe nanocrystals. *Nat. Mater.* **2016**, *15*, 1248–1254.
- (29) Wang, Y.; Peng, X.; Abelson, A.; Xiao, P.; Qian, C.; Yu, L.; Ophus, C.; Ercius, P.; Wang, L.; Law, M.; Zheng, H. Dynamic deformability of individual PbSe nanocrystals during superlattice phase transitions. *Science Advances* **2019**, *5*, eaaw5623.
- (30) Ou, Z.; Wang, Z.; Luo, B.; Luijten, E.; Chen, Q. Kinetic pathways of crystallization at the nanoscale. *Nat. Mater.* **2020**, *19*, 450–455.
- (31) Wu, L.; Willis, J.; McKay, I. S.; Diroll, B. T.; Qin, J.; Cargello, M.; Tassone, C. J. High temperature crystallization of nanocrystals into three dimensional superlattices. *Nature* **2017**, *548*, 197–201.
- (32) Li, B.; Zhou, D.; Han, Y. L. Assembly and phase transitions of colloidal crystals. *Nat. Rev. Mater.* **2016**, *1*, 15011.
- (33) Peng, Y.; Wang, F.; Wang, Z.; Alsayed, A. M.; Zhang, Z.; Yodh, A. G.; Han, Y. L. Two step nucleation mechanism in solid-solid phase transitions. *Nat. Mater.* **2015**, *14*, 101–108.

- (34) Wang, Z.; Bian, K.; Nagaoka, Y.; Fan, H.; Cao, Y. C. Regulating multiple variables to understand the nucleation and growth and transformation of PbS nanocrystal superlattices. *J. Am. Chem. Soc.* **2017**, *139* (41), 14476–14482.
- (35) Gerdes, F.; Volkmann, M.; Schliehe, C.; Bielewicz, T.; Klinke, C. Sculpting of lead sulfide nanoparticles by means of acetic acid and dichloromethane. *Z. Phys. Chem.* **2015**, 229, 139–151.
- (36) Wang, Z.; et al. Integrating in situ high pressure small and wide angle synchrotron X-ray scattering for exploiting new physics of nanoparticle supercrystals. *Rev. Sci. Instrum.* **2010**, *81*, 093902.
- (37) Huang, X.; et al. Understanding Fe<sub>3</sub>O<sub>4</sub> Nanocube Assembly with Reconstruction of a Consistent Superlattice Phase Diagram. *J. Am. Chem. Soc.* **2019**, *141*, 3198–3206.
- (38) Jiang, Z. GIXSGUI: a MATLAB toolbox for grazing-incidence X-ray scattering data visualization and reduction, and indexing of buried three-dimensional periodic nanostructured films. *J. Appl. Crystallogr.* **2015**, *48*, 917–926.
- (39) Lewis, D. J.; Zornberg, L. Z.; Carter, D. J. D.; Macfarlane, R. J. Single crystal Winterbottom constructions of nanoparticle superlattices. *Nat. Mater.* **2020**, *19*, 719–724.
- (40) Cahn, J. W. Transformation kinetics during continuous cooling. *Acta Metall.* **1956**, *4*, 572–575.
- (41) Petukhov, A. V.; Dolbnya, I. P.; Aarts, D. G. A. L.; Vroege, G. J.; Lekkerkerker, H. N. W. Bragg rods and multiple X-ray scattering in random-stacking colloidal crystals. *Phys. Rev. Lett.* **2003**, *90*, 028304.
- (42) Quan, Z.; Wu, D.; Zhu, J.; Evers, W. H.; Boncella, J. M.; Siebbeles, L. D. A.; Wang, Z.; Navrotsky, A.; Xu, H. Energy landscape of self-assembled superlattices of PbSe nanocrystals. *Proc. Natl. Acad. Sci. U. S. A.* **2014**, *111*, 9054–9057.
- (43) Lee, B.; Littrell, K.; Sha, Y.; Shevchenko, E. V. Revealing the Effects of the Non-solvent on the ligand shell of nanoparticles and their crystallization. *J. Am. Chem. Soc.* **2019**, *141*, 16651–16662.
- (44) Deng, K.; Huang, X.; Liu, Y.; Xu, L.; Li, R.; Tang, J.; Lei, Q.; Ni, R.; Li, C.; Zhao, Y. S.; Xu, H.; Wang, Z.; Quan, Z. Supercrystallographic reconstruction of 3D nanorod assembly with collectively anisotropic upconversion fluorescence. *Nano Lett.* **2020**, 20, 7367–7374.